PHILOSOPHICAL TRANSACTIONS OF THE ROYAL SOCIETY A

rsta.royalsocietypublishing.org

Review

Cite this article: Levitas VI. 2013 Mechanochemical mechanism for reaction of aluminium nano- and micrometre-scale particles. Phil Trans R Soc A 371: 20120215. http://dx.doi.org/10.1098/rsta.2012.0215

One contribution of 13 to a Theme Issue 'Turbulent mixing and beyond: non-equilibrium processes from atomistic to astrophysical scales II'.

Subject Areas:
mechanical engineering, materials science

Keywords:
melt-dispersion mechanism, oxidation, flame propagation, melting, cavitation, stresses and fracture

Author for correspondence:
Valery I. Levitas
e-mail: vlevitas@iastate.edu

Mechanochemical mechanism for reaction of aluminium nano- and micrometre-scale particles

Valery I. Levitas

Departments of Aerospace Engineering, Mechanical Engineering, and Material Science and Engineering, Iowa State University, Ames, IA 50011, USA

A recently suggested melt-dispersion mechanism (MDM) for fast reaction of aluminium (Al) nano- and a few micrometre-scale particles during fast heating is reviewed. Volume expansion of 6% during Al melting produces pressure of several GPa in a core and tensile hoop stresses of 10 GPa in an oxide shell. Such stresses cause dynamic fracture and spallation of the shell. After spallation, an unloading wave propagates to the centre of the particle and creates a tensile pressure of 3–8 GPa. Such a tensile pressure exceeds the cavitation strength of liquid Al and disperses the melt into small, bare clusters (fragments) that fly at a high velocity. Reaction of the clusters is not limited by diffusion through a pre-existing oxide shell. Some theoretical and experimental results related to the MDM are presented. Various theoretical predictions based on the MDM are in good qualitative and quantitative agreement with experiments, which resolves some basic puzzles in combustion of Al particles. Methods to control and improve reactivity of Al particles are formulated, which are exactly opposite to the current trends based on diffusion mechanism. Some of these suggestions have experimental confirmation.

1. Melt-dispersion mechanism

Aluminium (Al) particles are becoming integrated into various energetic formulations, using the reaction heat of Al oxidation. When the diameter of the Al particle reduces to 20–120 nm (in contrast to traditional 10–100 μm size), their reactivity drastically increases. Thus, flame-propagation rates reach 1 km s^{-1}

Royal Society Publishing
Informing the science of the future

for reactive nanocomposites (e.g. Al + MoO_3 and Al + Fe_2O_3 nanopowder) in contrast to 1 m s^{-1} for micrometre-size Al particles [1,2], and ignition delay times are reduced by three orders of magnitude [3]. That is why Al nanoparticles became the most popular representatives of nanoenergetic materials. Because the Al particle is covered by an initial oxide shell of 2–7 nm width, reaction is governed by diffusion of oxygen and Al towards each other through the growing oxide shell [4,5]. However, there were a number of strong indications that the diffusion mechanism is far too slow to support a flame rate of 1 km s^{-1}. In particular, the diffusion length for oxygen and Al during the estimated reaction time for nanoparticles of $t_r = 10\,\mu$s is five orders of magnitude smaller than the initial shell thickness [6]. At the same time in experiments at 900°C, reaction time for even bare Al particles with a diameter $d = 20$ nm exceeds 1 s [7]. In addition, the flame speed and ignition time delay became independent of particle size for $d < 120$ nm [1,3,8]; for the diffusion oxidation mechanism, they are a power function of the diameter [3,9].

Because of the aforementioned contradictions between the diffusion mechanism and experimental data (as well as other ones that will be discussed below), the author suggested [6,10] a new mechanochemical mechanism called the *melt-dispersion mechanism* (MDM; figure 1) that explains the above puzzles and high reactivity of Al nanoparticles, as well as allows us to make a number of predictions. Thus, melting of Al is accompanied by a 6% volume increase and causes compressive pressure of several GPa in Al core and tensile hoop stresses of the order of 10 GPa in the shell. Such high tensile stresses cause fast fracture and spallation of the shell. Immediately after spallation, pressure inside the liquid Al particle remains the same (several GPa), whereas at the bare Al surface, it drops down to 10 MPa owing to surface tension and gas pressure [6]. The sudden pressure drop at the Al surface creates an unloading wave with a tensile pressure in the range of 3–8 GPa, which disperses Al particles into a large number of small, bare Al fragments (clusters). Oxidation of these clusters is not limited by diffusion through the initial oxide shell. Thus, MDM transforms single particles covered by oxide shell into hundreds or thousands smaller bare particles, which explains the drastic increase in particle reactivity.

In the paper, we review the current state of development of the MDM, related modelling, experimental verification, as well as predictions for the improvement of reactivity of nano- and micrometre Al particles. Owing to the short process time and small particle size, there are no *in situ* experimental observations of the MDM. However, we developed a theory and made various predictions, the majority of which are in good qualitative or even quantitative agreement with experiments. In addition, because predictions based on the diffusion mechanism and MDM are opposite, it is easy to determine which of them corresponds to experimental data.

2. Stress development and fracture in a core–shell system

A simple spherical model of an Al particle of radius R, covered by a shell of thickness δ, is considered under action of gas pressure p_g (figure 1). The core consists of a melt with volume concentration f and solid with concentration $1-f$. Pressure in the Al core, p, and maximum tensile hoop stresses in a shell at the interface with the Al sphere, σ_h, have been found in [6,13]:

$$p = \frac{12(m^3-1)(\varepsilon_2^i-\varepsilon_1^i)G_2K_1K_2}{H} + \frac{2K_1(4G_2+3m^3K_2)\Gamma_1}{RH} + \frac{(2\Gamma_2+p_gRm)m^2K_1(4G_2+3K_2)}{RH}; \quad (2.1)$$

and

$$\sigma_h = -\frac{6(m^3+2)(\varepsilon_2^i-\varepsilon_1^i)G_2K_1K_2}{H} + \frac{4(m^3+2)G_2K_2\Gamma_1}{RH} + \frac{(2\Gamma_2+p_gRm)m^2(-2G_2K_1+3(2G_2+K_1)K_2)}{RH}, \quad (2.2)$$

where $H = 3m^3K_1K_2 + 4G_2(K_1+(m^3-1)K_2)$, subscripts 1 and 2 designate Al and alumina, respectively, $m = 1+1/M$, $M = R/\delta$, G and K are the shear and bulk moduli, $K_1 = fK_1^m + (1-f)K_1^s$

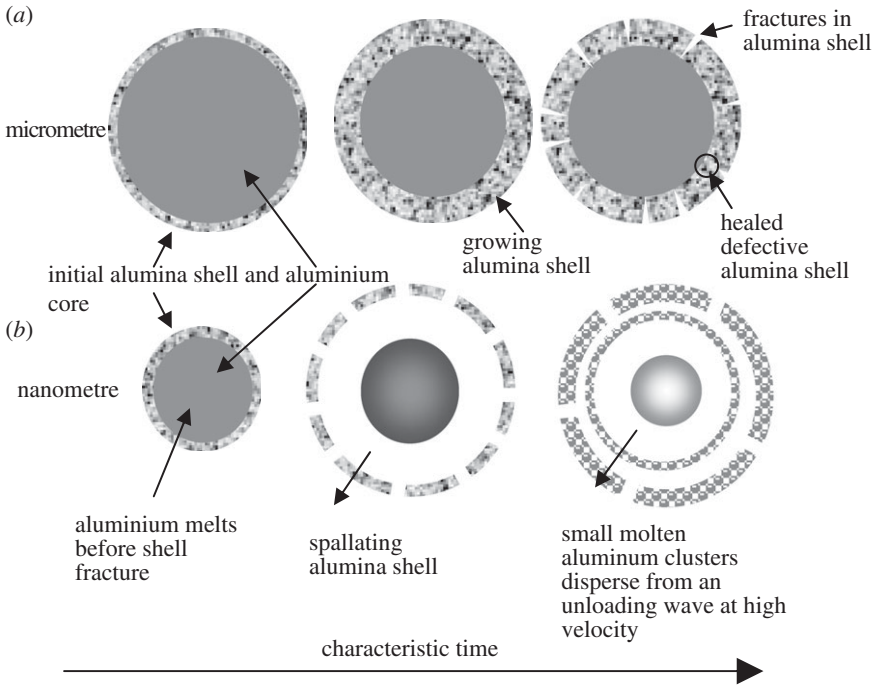

Figure 1. (*a*) Scheme of oxidation of Al micrometre-scale particles by diffusion of atoms through an oxide shell, which fractures before Al melting and then heals [5,11,12]. (*b*) Scheme of Al nanoparticle reaction by a melt-dispersion mechanism. Reproduced from [6].

is the bulk modulus of Al liquid–solid mixture, subscripts s and m are for the solid and melt phases, Γ_1 and Γ_2 are the surface energies at the core–shell and shell–gas interfaces. It is accepted that tensile stress is negative and compressive stress is positive. Inelastic strain consists of thermal and transformational parts:

$$\left.\begin{aligned} \varepsilon_1^i &= -(\alpha_s(T_m - T_0) + (1-f)\alpha_s(T - T_m) + f\alpha_m(T - T_m) + f\varepsilon^m) \\ \text{and} \qquad \varepsilon_2^i &= -\alpha_2(T - T_0), \end{aligned}\right\} \tag{2.3}$$

where α is the linear thermal expansion coefficient, T_0 is the temperature at which internal thermal stresses in the solid state are zero, and $3\varepsilon^m$ is the volumetric expansion during the melting of Al. The shell fractures when the fracture criterion, $-\sigma_h = \sigma_u$, is met, where σ_u is the ultimate strength of alumina. All material parameters are presented in reference [6]. With increasing volume fraction of melt in a core, both pressure and hoop stress grow until the fracture criterion is met and the shell fractures and spallates. Substituting equations (2.2)–(2.3) into the fracture criterion and solving for the concentration of melt in the Al core necessary to fracture the oxide shell at $T = T_m = 933.67$ K, we obtain [8,14]:

$$f = \frac{\left(-B + \sqrt{B^2 - 4AC}\right)}{2A}, \tag{2.4}$$

with $A = 6\delta\varepsilon^m\ \Delta K(2+m^3)MG_2K_2$, $B = \Delta Km^2(\delta(1+M)p_g + 2\Gamma_2)(2G_2 - 3K_2) + 6\delta(2+m^3)M(\varepsilon^m K_s + \Delta\alpha\Delta K\Delta T)G_2K_2 - \delta\Delta KM(4G_2 + 3m^3K_2)\sigma_u$, $C = 6\delta(2+m^3)M\Delta\alpha K_s\Delta TG_2K_2 - 4(2+m^3)\Gamma_1G_2K_2 + m^2(\delta(1+M)p_g + 2\Gamma_2)(2K_sG_2 - 3(K_s + 2G_2)K_2) - M\delta\sigma_u(3K_sK_2m^3 + 4G_2(K_s + (m^3-1)K_2))$.

In this equation, $\Delta K = K_m - K_s$, $\Delta T = T_m - T_0$ and $\Delta\alpha = \alpha_s - \alpha_2$. Figure 2 represents calculated relationships for f, necessary to induce fracture of the shell, versus relative particle size M, for various oxide shell strengths (shown near the curves in terms of fractions of the estimated

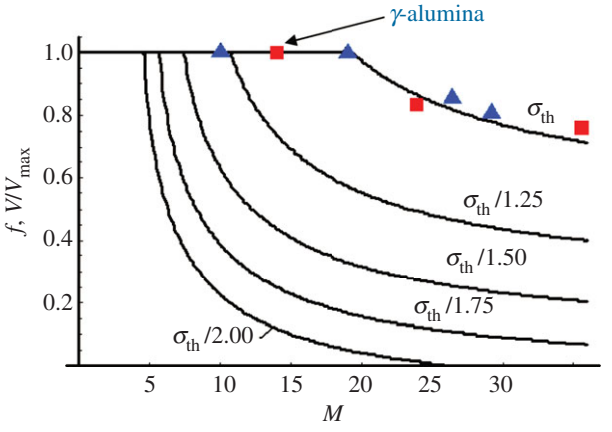

Figure 2. Relative flame speed versus $M = R/\delta$ [8,15]. For various oxide shell strengths (shown near the curves), the lines correspond to the concentration of melt, f, necessary to fracture the oxide shell. Marked point is obtained for shell in γ-phase; other points are for amorphous shell. Good correspondence between V/V_{max} and f is observed. (Online version in colour.)

value of theoretical strength $\sigma_{th} = E/30 = 11.33\,\text{GPa}$). We used $T_0 = 300\,\text{K}$ and $p_g = 0$. It can be seen that at some value of M for each ultimate strength, $f = 1$; i.e. the shell fractures after melting of the entire particle.

3. Relationship for the flame rate

When in experiment one fixes all parameters and reduces the particle size R or relative particle size M only, the flame rate reaches its maximum value V_{max} and does not change (figures 2 and 3). It is natural to assume that the entire melt that causes fracture of the shell will be dispersed and will participate in the MDM during time scales of approximately 10 μs, i.e. while the flame front passes through. The remaining non-dispersed Al reacts over longer time scales and does not contribute to the flame rate V. Then, the relative flame rate, V/V_{max}, should be an increasing function of the concentration of the melt in the particle, f, and the simplest linear relationship $V/V_{max} = f$ is checked first. In figure 2, experimental data for V from figure 3 are presented in the form V/V_{max} versus M and superposed onto plot $f(M)$. One can see practically perfect coincidence, which results in the following relation [8]:

$$\frac{V}{V_{max}} = f = \frac{(-B + \sqrt{B^2 - 4AC})}{2A} \quad \text{for} \quad 0 < f \le 1. \tag{3.1}$$

It is clear that an unambiguous relationship between the flame-propagation rate and particle size (which follows from the diffusion mechanism) does not exist, whereas the flame speed is determined by $M = R/\delta$. Equation (3.1) explains why the flame speed reaches its possible maximum, which is difficult to understand within diffusion mechanism. For particles with $d = 50$ and 120 nm, increase in shell thickness increases flame speed. Note that ignition delay time is also found to be independent of M below some critical $M < 17$, independent of specific R and δ [6]. In addition, results in reference [16] show that Al particles covered by an alumina shell have the flame rate higher by a factor of 22–95 in comparison with the particles without shell. All of these results contradict the diffusive mechanism but strongly support MDM.

Equation (3.1) implies that volume fraction of melt in a particle that causes fracture of the shell and then participates in the MDM is a new physical parameter controlling relative flame rate. It also suggests that other processes (melting, wave propagation, mixing with the oxidizer and cavitation of the molten Al) are not the limiting ones in the considered range of parameters, because the entire molten Al contributes to the oxidation reaction and flame rate V/V_{max}.

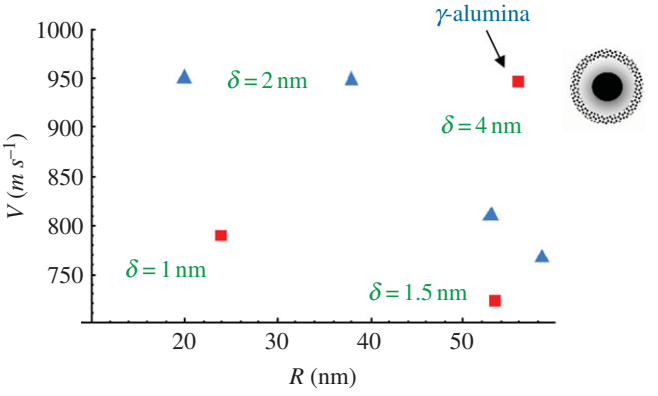

Figure 3. Flame speed versus Al particle core radius for several oxide thicknesses [8,15]. It is evident that there is no relationship between flame speed and particle size. The triangles ($\delta = 2$ nm) and squares correspond to data from [1] and [8], respectively. (Online version in colour.)

Equation (3.1) allows one to optimize flame speed for the chosen application. Because predictions based on the MDM are exactly opposite to those based on the diffusion mechanism, the directions in which the Al nanoparticle synthesis progresses are completely changed (see §9).

4. Tensile pressure wave, cavitation and the effect of heating rate

An aluminium sphere of radius R is considered, which is initially in equilibrium under an applied external pressure p_0, determined from equation (2.1). The pressure at the boundary $r = R$ linearly reduces in time from p_0 to the final value $p_f = 2\Gamma_2/R + p_g$ during the oxide fracture time t_s, after which it does not change. Analytical solution of the wave propagation problem is found in reference [6], including explicit expressions for maximum tensile pressure and particle velocity. Let $t_p = R/c$ be an acoustic time during which the wave reaches the centre of the sphere, where c is the sound velocity. As $c = 4166\,\mathrm{m\,s^{-1}}$, $t_p = 10$ ps for $R = 41.66$ nm. We found from phase-field [17] and molecular-dynamic modelling [18] that cavitation starts in the reflected wave in the central region of a particle. The maximum tensile (negative) pressure at the centre of the particle in the reflecting wave, p_{max}, is

$$p_{max} = p_0\left(1 - 2\frac{1-\bar{p}_f}{\bar{t}_s}\right), \tag{4.1}$$

and exceeds 8 GPa. The solution is confirmed by finite-element simulations [17]. The magnitude of p_{max} increases in inverse proportion with the shell fracture time. It is accepted in reference [6] that fracture occurs when negative pressure is smaller than the critical tensile pressure, p_c: $p_{max} \le p_c < 0$. Substituting equation (4.1) in the cavitation criterion results in the condition

$$\bar{t}_s \le 2\frac{1-p_f/p_0}{1-p_c/p_0}. \tag{4.2}$$

The smaller $\bar{t}_s = t_s/t_p$, i.e. the oxide shell fracture time relative to acoustic time, the lower the tensile pressure and, consequently, the initial compressive pressure that is required for cavitation. Thus, for $p_f/p_0 = 0.05$ one obtains

$$-\frac{p_0}{p_c} = 1 \quad \text{for} \quad t_s \le 0.95; \quad -\frac{p_0}{p_c} = 0.25 \quad \text{for} \quad \bar{t}_s \le 0.38 \quad \text{and} \quad -\frac{p_0}{p_c} = 0.1 \quad \text{for} \quad \bar{t}_s \le 0.18. \tag{4.3}$$

Thus, even if initial compressive pressure in the melt at the instant of shell fracture is 10 times smaller than the cavitation threshold, cavitation is still possible, provided that the fracture time is five times shorter than the acoustic time. Such fast fracture can be caused by *very fast heating only* and limits the range of parameters for which the MDM is active. Fast heating is

also important for fast melting of the particle and for overloading the entire oxide shell, which causes fast homogeneous fracture and spallation of the shell. This result allowed us to explain in reference [19] a paradoxical effect of the heating rate on burn time of Al nanoparticles. Thus, with a heating rate of the order of $10^3\,\mathrm{K\,s^{-1}}$, holding bare Al nanoparticles with $d = 50\,\mathrm{nm}$ for 1 s at $T = 1100^\circ\mathrm{C}$ results in only 4% of the particles being completely oxidized [7]; holding bare Al nanoparticles with $d = 20\,\mathrm{nm}$ for 1 s at $T = 900^\circ\mathrm{C}$ resulted in 68% of completely oxidized particles. The diffusive oxidation mechanism is confirmed by transmission electron microscopy (TEM) and theoretical modelling in reference [5]. On the other hand, after fast heating (estimated above $10^7\,\mathrm{K\,s^{-1}}$), the burn time of Al particles with $d = 80\,\mathrm{nm}$ at 1100°C was less than 500 μs only [20,21]. These results have been explained by the MDM. Indeed, the MDM requires high heating rates [6,19], and it cannot be activated at $10^3\,\mathrm{K\,s^{-1}}$; that is why slow diffusion-controlled oxidation occurs. However, heating at $10^7\,\mathrm{K\,s^{-1}}$ is sufficient to activate the MDM, which explains oxidation at 10–100 μs time scale.

An approximate estimate of the *heating rate* of $10^6\,\mathrm{K\,s^{-1}}$ necessary for activation of the MDM was performed in reference [19]. This heating rate corresponds to the *flame speed* of $10\,\mathrm{m\,s^{-1}}$. Note that in experiments [20,21], in which convective flow is absent and particles do not interact with one another, one may expect higher heating rates for initiation of MDM. It follows also from this result that owing to a change in mechanism, reactivity studies at small heating rates (*in situ* TEM, differential scanning calorimetry and thermogravimetry) cannot be correlated with burning in fast flame and under high heating rates. A rough *estimate of* the *cluster size* was made in reference [19] and it is of the order of 5–10 nm.

Note that a very advanced MD simulations of oxidation of Al nanoparticles was presented in reference [22] without and in reference [23] with initial oxide shell. However, these results cannot be compared with MDM, because the time scale in the MD simulations was 200 ps, and to obtain reaction during this time, both the concentration of oxygen and the temperature were increased to values of 6000–9000 K, which is much higher than in experiments in a burn tube. These MD simulations may be relevant for explanation of the experiments in references [24,25], in which estimated temperature is in the range 4500–8000 K.

5. Melting and surface melting of nanoparticles

For slow heating rates typical of differential scanning calorimetry measurements, the melting temperature of bare Al nanoparticles exhibits traditional depression proportional to $1/R$ [26,27]. However, it is relatively small: for example, it is 23 K for $R = 10\,\mathrm{nm}$. Melting within oxide shell leads to generation of internal pressure [28,29], which increases melting temperature by 55 K per GPa [30]. In reference [28], equation (2.1) was used to evaluate pressure in melt and its effect on the melting temperature versus experimental data. It was found that pressure generated by a difference in thermal expansion coefficients relaxes, and only pressure owing to the surface tensions at the Al–alumina and alumina–gas interfaces remains and increases the melting temperature. Damage to the oxide shell reduces pressure in melt and corresponding increase in melting temperature, which also allows one to quantify damage by the change in melting temperature. The possible stress relaxation mechanisms may be related to diffusion of Al into the shell, damage and diffusion-controlled creep of the oxide shell, and phase transformation from amorphous to crystalline phases in the alumina. However, because even volume increase owing to complete melting did not fracture the shell for particles with $R = 8.5\,\mathrm{nm}$ [28], the relaxation of thermal stress during heating below the melting temperature cannot be explained by damage to the oxide shell. In addition, because the shell of these particles does not transform from amorphous to γ-phase, phase transformation cannot be the only mechanism for stress relaxation. Thus, diffusion and related creep are currently the most probable candidates for stress relaxation mechanisms.

An additional reduction in melting temperature is related to the reduction in the total surface energy during melting, which causes surface melting [31]. For bulk Al, surface melting starts 50 K below the melting temperature [32], and the molten layer grows with increasing temperature.

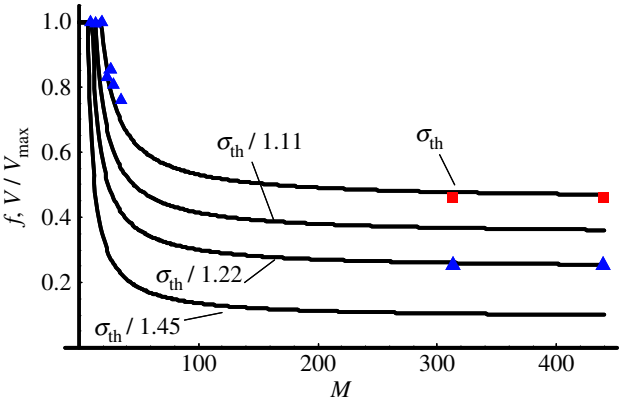

Figure 4. Relative flame velocity V/V_{max} versus $M = R/\delta$ for Al/teflon mixtures (squares) and Al/MoO_3 mixtures (triangles). The lines are based on equation (3.1) for the melt concentration, f, necessary to fracture the shell for various oxide shell strengths (shown near the curves). Adapted from [35]. Data for $M < 35$ are from [8]. (Online version in colour.)

An advanced phase-field model for melting coupled to mechanics was developed in references [33,34]. It describes well experimental data on the temperature-dependence of the thickness of the molten layer for a bulk sample and the melting temperature versus R for bare Al particles down to $R = 2$ nm. This makes plausible the results obtained in references [33,34] for surface melting of Al nanoparticles. Note that the results for slow heating are important for understanding and optimizing processes relevant to synthesis of Al particles (see §8).

For fast heating rates of 10^6–10^8 K s^{-1} typical of MDM, the stress relaxation owing to diffusion and creep may be neglected. In addition, phase transformation in the shell does not have time to occur [15]. Based on a simple analytical model, it was found in reference [6] that thermal conductivity is not a limiting process for MDM from the point of view of temperature heterogeneity. Indeed, for the heating rate of 10^8 K s^{-1}, the temperature at the surface is higher than that at the centre by less than 1 K for $R < 2.88$ μm and less than 10 K for $R < 9.12$ μm. Melting temperature increases at fast heating rates. Using phase-field model [34], it was obtained that bare Al particle with $R = 40$ nm at a heating rate of 10^8 K s^{-1} starts pre-melting at 893 K, and the interface propagates to the centre at $T = 932$ K.

In the analytical model for the prediction of the flame rate (see [6,15] and §3), all these details are neglected, and melting is assumed at $T_m = 933.67$ K. However, understanding of melting may lead to new ways to control the MDM. This is especially important for micrometre particles, for which the shell fractures at partial melting of the core. Thus, melting temperature can be reduced by reduction in pressure in an unloading wave. In addition, the solid–liquid interface is the probable site for the heterogeneous nucleation of cavitation. The melting rate determines the strain rate in the oxide shell [6], which is important for its fast fracture required for the MDM. Thus, the hoop strain rate in the shell is estimated as 3×10^4 s^{-1} [6].

6. Melt-dispersion mechanism for micrometre-scale particles and fluorination

Extending plot $f(M)$ for large M (figure 4), it is getting evident that if MDM is activated, micrometre Al particles can produce a high flame rate of $0.5\,V_{max}$. To check this prediction, experiments have been performed [27,35] with either 50 nm Al powder or 1–3 μm Al particles mixed with nanoscale MoO_3 or teflon. The micrometre-scale Al particles had a very broad size distribution and contained a number of Al nanoparticles, which may be important for the activation of MDM (see below). Experimental results for Al + teflon are in good agreement with the relationship $f(M)$ in the range $M = 312$–438, which *strongly supports the MDM* for 1–3 μm particles. This also means that the *cavitation of molten Al is not a rate-limiting process* even for

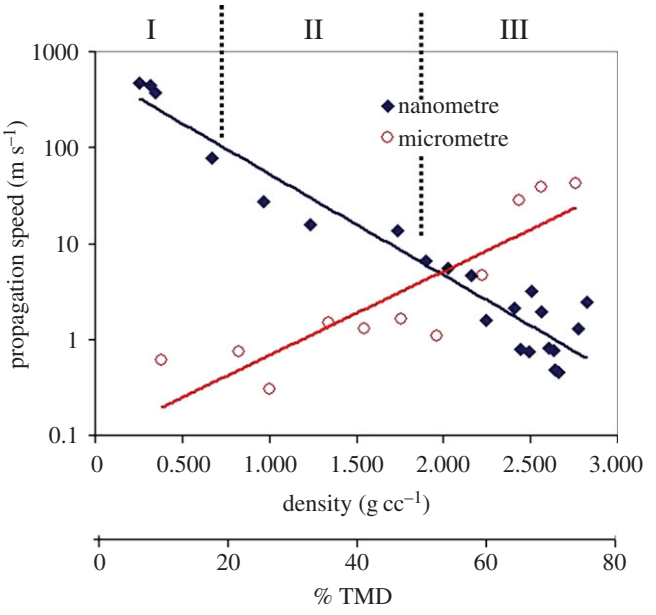

Figure 5. Flame speed as a function of mass density and theoretical mass density (TMD) for nano- or micro-scale Al particles mixed with nano-MoO_3. In regions I and II, the decrease in the flame rate is due to suppression of the MDM because of pressing-induced damage. In region III, the flame speed for nanoparticles is smaller than for micrometre-scale particles because of multiple barriers to diffusion due to multiple oxide shells along the diffusion path. Adapted with changes from [36,37]. (Online version in colour.)

micrometre particles. At the same time, the flame rate for Al + MoO_3 mixture is only 0.55 of the prediction of equation (3.1), which was explained by lower gas generation in comparison with teflon: the collision and reaction rates of Al fragments with gaseous oxygen may be a rate-limiting process.

7. The effect of damage to the shell on flame propagation for nano- and micrometre-scale composites

Paradoxical experimental results for Al + MoO_3 composites have been obtained in reference [36] and interpreted in references [6,37]. Reactive mixtures with micrometre-scale Al particles demonstrate an increase in flame-propagation rate with increased bulk density, whereas nanoparticles exhibit the opposite trend (figure 5). The dependence of the flame rate for micrometre particles is consistent with the diffusive reaction mechanism and the conductive flame-propagation mode. During pressing of the mixture to increase its density, the damage occurs to the oxide shell that accelerates diffusion of oxygen and/or Al and, consequently, the oxidation. In addition, the increase in contact area between the Al particles and the oxidizer also accelerates diffusion, as well as increases the thermal diffusivity of the mixture, leading to the faster conductive flame-propagation mode.

The results for nanoparticles are consistent with an MDM and convective mode [38] of flame propagation. The damage to the shell and distortion of the shape of spherical particles during compaction suppress the MDM. Reduced free space around Al nanoparticles suppresses both the MDM and the convective mode of flame propagation. Damage to the shell reduces the strength of the shell and, consequently, also decreases the pressure in a molten Al and volume fraction of melt, f, which is required for fracture of oxide shell. This reduces flame velocity according to equation (3.1) and figure 2. We found that compression and torsion of nanoparticles leads

to the reduction in flame speed from 342 ± 11 to $174 \pm 7\,\mathrm{m\,s^{-1}}$ for loose reactive mixture [6]. This supports our interpretation that deformation of nanoparticles, even without change in the sample density, leads to a reduction in the flame-propagation rate. At the same time, vibrational compaction should not damage the shell and suppress the MDM. Indeed, vibrational change in density in the range of 5–10% of TMD did not change the flame speed essentially [1]. The results related to the damage to the shell indirectly support the MDM versus the diffusional mechanism because predictions based on the two mechanisms are opposite.

8. Recommendations for improving the reactivity of aluminium particles

Based on the above results for the MDM, our ultimate goal is to design and synthesize an optimal micrometre-scale Al core–strong shell particle that transforms in flame into multiple nanoscale bare fragments that react as the best nanoparticles. The cost of micrometre-scale particles is 30–50 times smaller than nanoparticles and they do not have safety and environmental issues typical of nanoparticles. This goal and most of our predictions are opposite to the current trends based on diffusion mechanism. Based on the developed models and hypotheses, the main conditions for activation of the MDM were determined, and the controlling physical and geometric parameters are found. The effect of each controlling parameter is analysed, and some of our predictions are confirmed experimentally. Below, we enumerate our suggestions.

1. Recently [39], direct evidence of the MDM was proposed. After fast heating of Al nanoparticles with a flash-pulse, TEM images of particles with ruptured shells as well as small reacted clusters from the dispersion have been demonstrated.
2. According to equations (2.4)–(3.1) and figures 2 and 3, the ratio of particle radius to shell thickness $M = R/\delta$ (rather than R and δ separately) affects the flame velocity. To maximize flame rate, one has to choose $M = 19$. Decreasing M below 19 does not increase flame-propagation speed but increases the percentage of alumina in a particle, i.e. dead weight. It is reasonable to increase δ (and the particle radius) up to the maximum size for which it still possesses theoretical strength, which is at least 7.7 nm according to experiments and interpretation in references [3,6]. Then, the maximum value of $R = 19 \times 7.7 = 146$ nm was obtained, for which complete melting is expected before fracture of the oxide shell. Conceptual experimental confirmation of this trend is presented in figures 2 and 3, in which an increase in oxide width from 2 to 4 nm allowed us to increase the diameter of the Al nanoparticle for which the V reached its maximum value from 80 to 120 nm.
3. For micrometre-size particles, starting with some M, flame velocity weakly depends on M (figure 4), and for $M \to \infty$ and all material constants used in the paper, equations (2.4)–(3.1) transform to $V/V_{\max} = f = -1.052 + 0.103\,\sigma_u + 0.001127\,T_0$. For the chosen parameters σ_u and T_0, flame rate cannot be increased, but by increasing M one reduces the dead weight. The maximum value of M for which MDM can be activated is limited by cavitation and the possibility of heating the particle quasi-homogeneously with the required heating rate. The current maximum value reached experimentally for which equation (3.1) works is $M = 438$ for $d = 3\,\mu$m (see §6 and [15,16,35]).
4. Currently, the shell forms at room temperature T_r and the temperature at which particles is stress-free, $T_0 = T_\mathrm{r}$. An increase in T_0 creates initial tensile stresses in the core and compressive stresses in the oxide shell, which should suppress the initiation of fracture in the shell during heating and increase flame speed (see equations (2.1)–(3.1)). Our calculations in reference [6] demonstrate the following increase in $M_{\max}$ and $R_{\max}$ with the growth of T_0 for $\delta = 7.7$ nm:

$$T_0 = 300\,\mathrm{K} \to M_{\max} = 19 \to R_{\max} = 146\,\mathrm{nm}; \quad T_0 = 450\,\mathrm{K} \to M_{\max} = 29 \to R_{\max} = 223\,\mathrm{nm};$$

$$T_0 = 600\,\mathrm{K} \to M_{\max} = 52 \to R_{\max} = 400\,\mathrm{nm}; \quad T_0 = 785\,\mathrm{K} \to M_{\max} = \infty \to R_{\max} = \infty.$$

Thus, an increase in T_0 is one of the promising ways to expand the MDM to larger Al particles. The maximum T_0 increase is limited by a decohesion of the shell from the

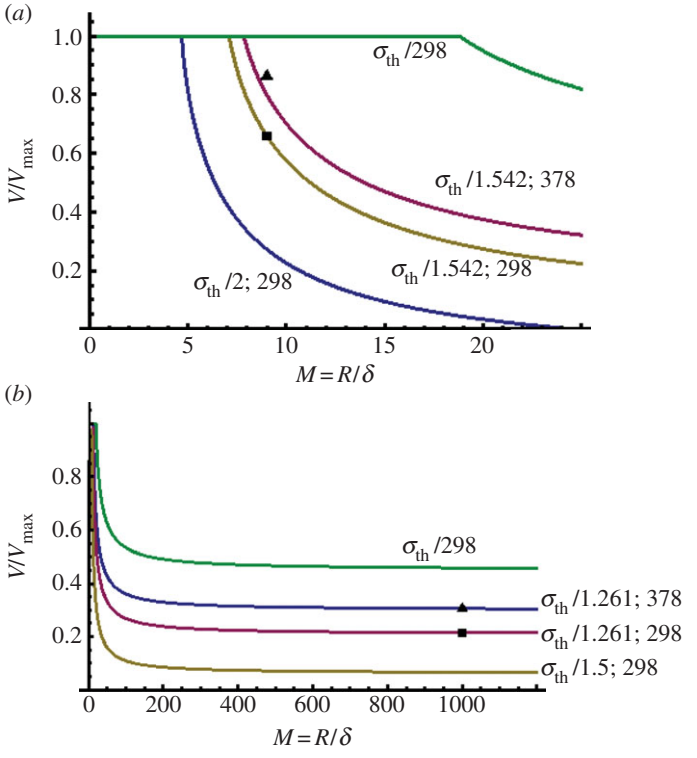

Figure 6. (*a–b*) Relative flame velocity V/V_{max} as a function of M for different values of the ultimate strength of the oxide shell (as a fraction of σ_{th}) and temperature T_0 (K), shown near the curves. Lines correspond to equations (2.4) and (3.1). Squares designate the experimental values for Al nanoparticles (left) and micrometre-scale particles (right) at $T_0 = 298$ K; triangles designate the experimental values at $T_0 = 378$ K. Quantitative agreement between theoretical predictions and experiments is evident. Adapted from [13]. (Online version in colour.)

Al core during cooling. The proof of concept for the design of pre-stressed Al nano- and micrometre particles was given in reference [13] for $Al + MoO_3$ reactive mixture. For the optimal pre-stressing conditions within the performed experiments, the flame rate increased by 31% for nanoparticles and by 41% for micrometre particles, both in quantitative agreement with theoretical predictions (figure 6). Further progress in this direction is related to fundamental understanding of the stress relaxation mechanisms, which includes both measurement and modelling of residual stresses.

5. *Porosity of the Al core*. A small degree of porosity within the core (1–4%, which is smaller than the 6% volume expansion during melting) will reduce stresses during melting and delay fracture of the shell. Equations (2.1) and (3.1) are applicable during the melting with substitution of ε^m with $\varepsilon^m - \varepsilon^v$, where $3\varepsilon^v$ is the porosity concentration. Porosity can be induced by using the Kirkendall effect during oxidation reaction [40,41]. Specifically, Al atoms diffuse to the shell and produce vacancies in the core, which coalesce into nanovoid. However, hollow Al particles were obtained for $d \leq 8$ nm only [40], and the it is not clear how to control void nucleation and growth in larger particles. A mechanochemical model for nucleation and growth of a nanovoid was developed in reference [42], where some ways to promote the growth of nanovoids have been suggested. Alternatively, reduction in pressure in melt can be achieved by alloying Al with some elements, which lead to reduction in ε^m.
6. According to equations (2.4) and (3.1), the increase in the strength of the shell increases in the flame-propagation rate. To reduce damage to the shell during pressing to high

density [37], one can reduce the loading force on individual particles. This could be done, for example, by combining nanoparticles with a liquid teflon binder and mould-casting the pellet, which is used by manufacturers of reactive materials (such as RM-4 by GSI) [37].

Alternatively, one can substitute alumina shell with stronger material, for example tungsten or tungsten oxides. In addition to an increase in σ_u, these materials may react with Al at high temperature, and thus they will not be considered as dead weight. In addition, tungsten as a heavy metal is important for reactive materials applications. Substituting alumina shell with protecting metals [43] or polymers [44] is one of the current trends in the development of nanoparticles. However, the shells were weaker than aluminium oxide, which should reduce flame-propagation speed, as we demonstrated for perfluoroalkyl carboxylic acid coating in reference [16]. For promoting the MDM, the protecting shell should be stronger than alumina.

7. Mixing of nano- and micrometre-scale particles, or, more generally, exploring the particle size distribution, may lead to improvement of the reactivity of a mixture. The heat generated by nanoparticles reacting via the *MDM* can increase temperature and heating rate for micrometre-scale particles and initiate the MDM in them. We believe that this was the reason for the high flame rate in micrometre-scale particles in references [15,35] (see §6). In addition, the pellets with 70% Al nanoparticles and 30% of 20 μm size particles, as well as loose powder with 70% Al nanoparticles and 30% micrometre particles with $d = 4$ and 20 μm, exhibit the same flame-propagation rate as Al nanoparticles alone [45].
8. In order to promote heterogeneous bubble nucleation and reduce the critical cavitation pressure, impurities should be added in the Al core. This recommendation is the opposite to the current trend to use high-purity Al.
9. By controlling properties of the Al–alumina interface, one can control melting temperature, strain rate in an oxide shell and the temperature at which the shell spallates. Currently, an incoherent, Al–amorphous alumina interface reduces its energy during melting, causing surface melting below T_m. In this case, melting occurs in some temperature ranges, which reduces the melting rate and strain rate in an oxide shell. If one can produce a low energy coherent interface between Al and crystalline alumina, its energy will grow during melting, and surface melting will be suppressed. Then, the fast heating may lead to significant (by several hundred degrees) overheating above T_m before melting starts. The melting rate will be much faster because of the higher temperature, which increases strain rate in a shell.

9. Conclusion

The main results in the development of the recently formulated MDM mechanism of reaction of Al nano- and a few micrometre-scale particles are reviewed in the current paper. Numerous non-trivial qualitative and quantitative confirmations of the predictions based on MDM strongly support this mechanism. It follows from equations (2.1)–(3.1) and figures 2, 4 and 6 that relative flame rate is equal to the concentration of the melt in a particle that is necessary for fracture of the shell. That means that the entire available melt participates in oxidation while the flame front passes through. This strongly supports the part of the MDM that involves equations (2.1)–(3.1). MDM allows us to resolve numerous puzzles in combustion of Al nanoparticles. MDM has a specific range of parameters and conditions for its activation, in particular some critical heating rate and strong shell. Outside of these regions, other oxidation mechanisms operate. Because currently these conditions are not strictly defined, lack of proof (or disproof) of MDM in some experiments does not contradict its existence under proper conditions.

Current trends in the improvement of Al particles based on diffusion mechanism are (i) to decrease the particle size; (ii) to reduce or completely eliminate the oxide shell; (iii) to damage the oxide shell; (iv) to keep the Al content high; (v) to passivate particles at room temperature;

(vi) to use high-purity Al; and (vii) to have narrow particle size distribution. Our results based on MDM change the directions of development of the Al particle to the opposite ones. Thus, one has

- to increase the oxide shell thickness to the maximum value at which it still possesses the maximum strength due to lack of defects;
- to increase the particle size up to the value $M = R/\delta$, which gives the maximum flame speed, or to the micrometre-scale size that has much lower cost than nanoparticles;
- to increase passivation temperature T_0 to the value that maximizes flame speed;
- to increase shell strength by substituting alumina with stronger oxide or metal;
- to use a mixture of nano- and micrometre-scale particles;
- to reduce the purity of Al (or to add inclusions) to reduce cavitation pressure;
- to control strain rate in a shell and temperature, at which Al melts and the shell breaks, by controlling the energy of the core–shell interface; and
- to reduce pressure in the molten core by introducing some porosity or by alloying Al with some elements, which leads to reduction in volume expansion during melting.

Some conceptual confirmations of our recommendations are summarized in §8.

Acknowledgements. The author thanks all his co-authors (collaborators and students) who are listed in references. The most productive collaboration on this topic the author has is with Dr M. L. Pantoya, who leads most of the experiments on justification of the MDM. Special thanks go to Drs B. W. Asay and S. F. Son. Discussions with Drs N. Glumac, M. Zachariah and K. Schroder are very much appreciated.

Funding statement. Support of the NSF (CBET-0755236 and CMMI-0969143), ONR, Air Force SBIR and Los Alamos National Laboratory is acknowledged.

References

1. Bockmon B, Pantoya M, Son S, Asay B, Mang J. 2005 Combustion velocities and propagation mechanisms of metastable interstitial composites. *J. Appl. Phys.* **98**, 064903. (doi:10.1063/1.2058175)
2. Plantier KB, Pantoya ML, Gash AE. 2005 Combustion wave speeds of nanocomposite Al/Fe_2O_3: the effects of Fe_2O_3 particle synthesis technique. *Combust. Flame* **140**, 299–309. (doi:10.1016/j.combustflame.2004.10.009)
3. Granier J, Pantoya M. 2004 Laser ignition of nanocomposite thermites. *Combust. Flame* **138**, 373–383. (doi:10.1016/j.combustflame.2004.05.006)
4. Dreizin EL. 2009 Metal-based reactive nanomaterials. *Prog. Energ. Combust.* **35**, 141–167. (doi:10.1016/j.pecs.2008.09.001)
5. Rai A, Park K, Zhou L, Zachariah M. 2006 Understanding the mechanism of aluminium nanoparticle oxidation. *Combust. Theor. Model.* **10**, 843–859. (doi:10.1080/13647830600800686)
6. Levitas VI, Asay BW, Son SF, Pantoya ML. 2007 Mechanochemical mechanism for fast reaction of metastable intermolecular composites based on dispersion of liquid metal. *J. Appl. Phys.* **101**, 1–20. (doi:10.1063/1.2720182)
7. Park K, Lee D, Rai A, Mukherjee D, Zachariah M. 2005 Size-resolved kinetic measurements of aluminum nanoparticle oxidation with single particle mass spectrometry. *J. Phys. Chem. B* **109**, 7290–7299. (doi:10.1021/jp048041v)
8. Levitas VI, Pantoya ML, Dikici B. 2008 Melt dispersion versus diffusive oxidation mechanism for aluminum nanoparticles: critical experiments and controlling parameters. *Appl. Phys. Lett.* **91**, 011921. (doi:10.1063/1.2824392)
9. Glassman I. 1977 *Combustion*. New York, NY: Academic Press.
10. Levitas VI, Asay BW, Son SF, Pantoya ML. 2006 Melt dispersion mechanism for fast reaction of nanothermites. *Appl. Phys. Lett.* **89**, 071909. (doi:10.1063/1.2335362)
11. Rozenband V, Vaganova NI. 1992 A strength model of heterogeneous ignition of metal particles. *Combust. Flame* **88**, 113–118. (doi:10.1016/0010-2180(92)90011-D)
12. Rozenband V. 2004 Thermo-mechanical aspects of the heterogeneous ignition of metals. *Combust. Flame* **137**, 366–375. (doi:10.1016/j.combustflame.2004.02.009)
13. Levitas VI, Dikici B, Pantoya ML. 2011 Toward design of the pre-stressed nano- and microscale aluminum particles covered by oxide shell. *Combust. Flame* 158, 1413–1417. (doi:10.1016/j.combustflame.2010.12.002)

14. Levitas VI, Pantoya ML. 2009 Mechanochemical mechanism for fast reaction of metastable intermolecular composites based on dispersion of liquid metal. *Int. J. Ener. Mater. Chem. Propulsion* **7**, 17–38.
15. Watson KW, Pantoya M, Levitas VI. 2008 Fast reactions with nano and micron aluminum: a study on oxidation versus fluorination. *Combust. Flame* **155**, 619–634. (doi:10.1016/j.combustflame.2008.06.003)
16. Dikici B, Dean SW, Pantoya ML, Levitas VI, Jouet RJ. 2009 Influence of aluminum passivation on the reaction mechanism: flame propagation studies. *Energy Fuels* **23**, 4231–4235. (doi:10.1021/ef801116x)
17. Levitas VI, Idesman AV, Palakala A. 2011 Phase field modeling of fracture in liquid. *J. Appl. Phys.* **110**, 033531. (doi:10.1063/1.3619807)
18. Levitas VI, Zhakhovskii V, Zybin SV. 2008 Dynamic fracture of liquid in an unloading wave within aluminum nanoparticle. Abstracts of the conference. In *New models and hydrocodes for shock wave processes in condensed matter* (ed. I Plaksin), pp. 122–123. Portugal: Estoril.
19. Levitas VI. 2009 Burn time of aluminum nanoparticles: strong effect of the heating rate and melt dispersion mechanism. *Combust. Flame* **156**, 543–546. (doi:10.1016/j.combustflame.2008.11.006)
20. Bazyn T, Krier H, Glumac N. 2006 Combustion of nanoaluminum at elevated pressure and temperature behind reflected shock waves. *Combust. Flame* **145**, 703–713. (doi:10.1016/j.combustflame.2005.12.017)
21. Bazyn T, Krier H, Glumac N. 2007 Evidence for the transition from the diffusion-limit in aluminum particle combustion. *Proc. Combust. Inst*. **31**, 2021–2028. (doi:10.1016/j.proci.2006.07.161)
22. Campbell TJ, Aral G, Ogata S, Kalia RK, Nakano A, Vashishta P. 2005 Oxidation of aluminum nanoclusters. *Phys. Rev. B* **71**, 205413. (doi:10.1103/PhysRevB.71.205413)
23. Wang WQ, Clark R, Nakano A, Kalia RK, Vashishta P. 2009 Fast reaction mechanism of a core(Al)-shell (Al2O3) nanoparticle in oxygen. *Appl. Phys. Lett*. **95**, 261901. (doi:10.1063/1.3268436)
24. Yang YQ, Wang SF, Sun ZY, Dlott DD. 2004 Propagation of shock-induced chemistry in nanoenergetic materials: the first micrometer. *J. Appl. Phys*. **95**, 3667–3676. (doi:10.1063/1.1652250)
25. Wang S, Yang Y, Yu H, Dlott DD. 2005 Dynamical effects of the oxide layer in aluminum nanoenergetic materials. *Propell. Explos. Pyrot*. **30**, 148–155. (doi:10.1002/prep.200400097)
26. Lai SL, Carlsson JRA, Allen LH. 1998 Melting point depression of Al clusters generated during the early stages of film growth: nanocalorimetry measurements. *Appl. Phys. Lett*. **72**, 1098–1100. (doi:10.1063/1.120946)
27. Eckert J, Holzer JC, Ahn CC, Fu Z, Johnson WL. 1993 Melting behavior of nanocrystalline aluminum powders. *Nanostruct. Mater*. **2**, 407–413. (doi:10.1016/0965-9773(93)90183-C)
28. Levitas VI, Pantoya M, Chauhan G, Rivero I. 2009 Effect of the alumina shell on the melting temperature depression for nano-aluminum particles. *J. Phys. Chem. C* **113**, 14088–14096. (doi:10.1021/jp902317m)
29. Sun J, Simon SL. 2007 The melting behavior of aluminum nanoparticles. *Thermochim. Acta* **463**, 32–40. (doi:10.1016/j.tca.2007.07.007)
30. Mei QS, Wang SC, Cong HT, Jin ZH, Lu K. 2005 Pressure-induced superheating of Al nanoparticles encapsulated in Al_2O_3 shells without epitaxial interface. *Acta Mater*. **53**, 1059–1066. (doi:10.1016/j.actamat.2004.11.003)
31. Denier van der Gon AW, Smith RJ, Gay JM, O'Connor DJ, van der Veen JF. 1990 Melting of Al surfaces. *Surf. Sci*. **227**, 143–149. (doi:10.1016/0039-6028(90)90402-T)
32. Davitt K, Arvengas A, Caupin F. 2010 Water at the cavitation limit: density of the metastable liquid and size of the critical bubble. *EPL* **90**, 16002. (doi:10.1209/0295-5075/90/16002)
33. Levitas VI, Samani K. 2011 Size and mechanics effects in surface-induced melting of nanoparticles. *Nat. Commun*. **2**, 284. (doi:10.1038/ncomms1275)
34. Levitas VI, Samani K. 2011 Coherent solid–liquid interface with stress relaxation in a phase-field approach to the melting/freezing transition. *Phys. Rev. B, Rapid Commun.* **84**, 140103(R). (doi:10.1103/PhysRevB.84.140103)

35. Levitas VI, Pantoya ML, Watson KW. 2008 Melt dispersion mechanism for fast reaction of aluminum particles: extension for micron scale particles and fluorination. *Appl. Phys. Lett*. **92**, 201917. (doi:10.1063/1.2936855)
36. Pantoya ML, Granier JJ. 2005 Combustion behavior of highly energetic thermites: nano versus micron composites. *Propell. Explos. Pyrotech.* **30**, 53–62. (doi:10.1002/prep.200400085)
37. Pantoya ML, Levitas VI, Granier JJ, Henderson JB. 2009 The effect of bulk density on the reaction dynamics in nano and micron particulate thermites: alternative reaction and flame propagation mechanisms. *J. Propul. Power* **25**, 465–470. (doi:10.2514/1.36436)
38. Sanders VE, Asay BW, Foley TJ, Tappan BC, Pacheco AN, Son SF. 2007 Reaction propagation of four nanoscale energetic composites (Al/MoO_3, Al/WO_3, Al/CuO, and Bi_2O_3). *J. Propul. Power* **23**, 707–714. (doi:10.2514/1.26089)
39. Ohkura Y, Rao PM, Zheng X. 2011 Flash ignition of Al nanoparticles: mechanism and applications. *Combust. Flame* **158**, 2544–2548. (doi:10.1016/j.combustflame.2011.05.012)
40. Nakamura R, Tokozakura D, Nakajima H, Lee JG, Mori H. 2007 Hollow oxide formation by oxidation of Al and Cu nanoparticles. *J. Appl. Phys.* **101**, 074303. (doi:10.1063/1.2711383)
41. Yin YD, Rioux RM, Erdonmez CK, Hughes S, Somorjai GA, Alivisatos AP. 2004 Formation of hollow nanocrystals through the nanoscale Kirkendall Effect. *Science* **304**, 711–714. (doi:10.1126/science.1096566)
42. Levitas VI, Attariani H. 2012 Mechanochemical continuum modeling of nanovoid nucleation and growth in reacting nanoparticles. *J. Phys. Chem. C* **116**, 54–62. (doi:10.1021/jp2055365)
43. Foley TJ, Johnson CE, Higa KT. 2005 Inhibition of oxide formation on aluminum nanoparticles by transition metal coating. *Chem. Mater.* **17**, 4086–4091. (doi:10.1021/cm047931k)
44. Jouet RJ, Warren AD, Rosenberg DM, Bellitto VJ, Park K, Zachariah MR. 2005 Surface passivation of bare aluminum nanoparticles using perfluoroalkyl carboxylic acids. *Chem. Mater.* **17**, 2987–2996. (doi:10.1021/cm048264y)
45. Moore K, Pantoya ML, Son SF. 2007 Combustion behaviors resulting from bimodal aluminum size distributions in thermites. *J. Propul. Power* **23**, 181–185. (doi:10.2514/1.20754)